Materials Horizons

ROYAL SOCIETY OF CHEMISTRY

COMMUNICATION

View Article Online
View Journal | View Issue

Cite this: *Mater. Horiz.*, 2022, 9, 2797

Received 9th June 2022,
Accepted 12th August 2022

DOI: 10.1039/d2mh00718e

rsc.li/materials-horizons

Ultra-stable self-standing Au nanowires/TiO_2 nanoporous membrane system for high-performance photoelectrochemical water splitting cells†

Ewa Wierzbicka, *[ab] Thorsten Schultz, [cd] Karolina Syrek, [e] Grzegorz Dariusz Sulka, [e] Norbert Koch [cd] and Nicola Pinna *[a]

We introduce for the first time a core–shell structure composed of nanostructured self-standing titania nanotubes (TNT, light absorber) filled with Au nanowire (AuNW) array (electrons collector) applied to the photoelectrocatalytic water splitting. Its activity is four times higher than that of reference TNT–Ti obtained with the same anodizing conditions. The composite photoanode brings a distinct photocurrent generation (8 mA cm^{-2} at 1.65 V *vs.* RHE), and a high incident photon to current efficiency of 35% obtained under UV light illumination. Moreover, the full system concept of selected constitutional materials, based on Au noble metal and the very stable semiconductor TiO_2, ensures a stable performance over a long-time range with no photocurrent loss during 100 on–off cycles of light illumination, after 12 h constant illumination and after one-month storage in air. We provide experimental evidence by photoelectron spectroscopy measurements, confirming that the electronic structure of TNT–AuNW is rectifying for electrons and ohmic for holes, while the electrochemical characterization confirms that the specific architecture of the photoanode supports electron separation due to the presence of a Schottky type contact and fast electron transport through the Au nanowires. Although the composite material shows an unchanged electrochemical band gap, typical for plain TiO_2, we find this material to be an innovative platform for efficient photoelectrochemical water splitting under UV light illumination, with significant potential for further modifications, for example extension into the visible light regime.

New concepts

Noble metal modifications of TiO_2 nanotubes photoanodes are popular, but typical strategies consider the top decoration of the oxide layer still attached to the Ti substrate. In this work, we introduce for the first time a novel synthesis method of a core-shell structure composed of nanostructured self-standing titania nanotubes (light absorber) filled with Au nanowires (electrons collector). The synthesis of thin self-standing TiO_2 itself is an original procedure, and it is further combined with Au nanowires electrodeposition. The photon to current efficiency of our photoanode reaches 35% and is four times higher than that of a reference obtained with the same anodizing conditions. The material shows incredible stability confirmed by no photocurrent loss during 100 on–off cycles of light illumination, after 12 h constant illumination, and after one-month storage in air. The reasons for such an improvement are attributed to the original architecture of the photoanode that promotes electron separation due to the presence of a Schottky type contact and fast electron transport through the Au nanowires.

Introduction

Hydrogen is the most prominent substitute for classic fossil fuels. It is an ideal zero-carbon footprint energy carrier (combustion with oxygen produces pure water) that has a complete lack of negative drawbacks on the environment. Furthermore, it is characterized by the highest calorific value (120–142 MJ kg^{-1}) from all kinds of fuels (*e.g.*, second place methane 50–55 MJ kg^{-1}). Photoelectrochemical (PEC) water splitting (WS), using photosensitive materials, is one of the most promising and environmentally friendly approaches to solar energy utilization for the renewable production of hydrogen. This makes the task of finding new photosensitive materials suitable for hydrogen production timely and highly relevant.

TiO_2 is a benchmark semiconductor material that shows a high photocorrosion resistance, availability, low cost, and at the

[a] *Institut für Chemie and IRIS Adlershof, Humboldt-Universität zu Berlin, Brook-Taylor-Str. 2, 12489 Berlin, Germany. E-mail: nicola.pinna@hu-berlin.de*
[b] *Department of Functional Materials and Hydrogen Technology, Faculty of Advanced Technologies and Chemistry, Military University of Technology, 2 Kaliskiego Street, 00908 Warsaw, Poland. E-mail: ewa.wierzbicka@wat.edu.pl*
[c] *Institut für Physik and IRIS Adlershof, Humboldt-Universität zu Berlin, Brook-Taylor-Str. 6, 12489 Berlin, Germany*
[d] *Helmholtz-Zentrum Berlin für Materialien und Energie GmbH, Hahn-Meitner-Platz 1, 14109 Berlin, Germany*
[e] *Faculty of Chemistry, Jagiellonian University in Krakow, Gronostajowa 2, 30-387 Krakow, Poland*

† Electronic supplementary information (ESI) available. See DOI: https://doi.org/10.1039/d2mh00718e

same time is environmentally friendly. As an n-type semiconductor and due to its suitable energies of conduction band (CB) and valence band (VB) edges, it meets the necessary prerequisites for the solar-driven photolysis of water.[1,2] A simple approach that leads to the creation of strongly organized titania nanostructures in a form of parallel nanotubes (TNT) on a Ti substrate is self-ordering anodizing. This fabrication method is considered the most versatile approach for the generation of TiO_2 nanostructures, as its morphology (the diameter of the pores and the length of the TNTs) can be simply tailored by the anodizing parameters.[3,4] Such nanostructured oxide layers show a bunch of unique features beneficial for PEC applications, for example, it has a large total surface area available for reactions, incomparable higher than in compact materials.[5] The major drawback limiting the process's performance is the high band gap of the pure TiO_2 (only UV light absorption), recombination of photogenerated charges, and slow kinetics of reactions occurring on TiO_2/aqueous environment interfaces. To overcome these problems, it is beneficial to combine TiO_2 with secondary materials.

It is very well known, especially from photocatalytic (PC) studies on H_2 evolutions, that the most common and efficient approach of titania modification is coupling with noble metal cocatalysts such as Pt, Ag, Au[6–9] or their alloys.[10] Coupling of TiO_2 surface with noble metals typically results in a very high efficiency of PC and PEC processes, assigned to several different effects such as Schottky barrier (SB) formation,[11,12] co-catalytic properties, or surface plasmon resonance (SPR).[13–15] The processes that might take place at the metal-semiconductor interface are complex. The character of the observed effect is determined by the type of metal (*e.g.*, the junction type depends on the difference in the work functions of metal and TiO_2), but also more recently size-dependent behavior was found to be an important aspect to be considered (*e.g.*, single atoms,[16] metal clusters,[17,18] nanoparticles[6]).

In this work, we present a comprehensive synthesis method of a new type of photoanode architecture based on an anodic TNT freestanding membrane (detached from Ti) filled with Au nanowires (TNT–AuNW) for application in PEC water splitting. Various approaches have been reported in the literature to fabricate free-standing TNT membranes, such as mechanical detachment, potential shock, or chemical etching,[19] however, detachment of the assembled TNT–AuNW composite has not been reported yet. In this work, we have shown that the TNT membrane filling with metal nanowires results in strong system stability and allows for the preparation of as thin as a few micrometers TiO_2 membranes.

The specific TNT–AuNW architecture leads to an extremely large interface area between Au and TiO_2 that provides an enhanced spatial separation of holes and electrons into the opposite sides of the photoanode and fast electron transport. Here the role of the self-standing anodic TNT membrane is twofold: as absorbing material and as large surface area nanoporous scaffold for the sequential deposition of AuNWs.

Through the AuNW core electrodeposited inside the TNT shell, the photogenerated electrons are extracted *via* an antenna system into an external circuit. The Schottky type contact at the Au/TiO_2 interface has rectifying properties for electrons and ohmic for holes (in the dark and without an external potential applied).[20] In other words, there is no resistance on the interphase for holes, while electrons must overcome a small build-in potential between the semiconductor and the metal. This however can be rather easily overcome by photoexcited electrons in the conduction band.[21] The width of the depletion region can be also reduced by forward potential bias. Once the electrons move to the metal, the higher energy Schottky barrier in the opposite direction will prevent a return of the electrons to the semiconductor.[11,22–24] From this point, the electron transport is facilitated through the metal nanowires, minimizing recombination in contrast to migration through the polycrystalline semiconductor in which grain boundaries are recognized as major recombination centers.[25]

For the first time a synthesis method combining Au nanowires into self-standing TiO_2 nanoporous membranes as a photoanode material for PEC WS is presented here. The investigated composite material brings a fourfold photoelectrocatalytic enhancement in comparison to TNT grown on the Ti substrate. The photoanode material also shows a stable long-term performance in PES WS under UV illumination. To the best of our knowledge, such an approach has not been reported so far.

Experimental

Materials synthesis

TiO_2 nanotubes were synthesized by self-organized anodizing of a Ti foil (Advent, 0.125 mm thickness, purity 99.6+%). Prior to anodizing, the Ti substrates were degreased by 15 min sequential sonication in acetone, ethanol, and deionized water, followed by drying in a nitrogen stream. The non-working area of the sample was insulated with a peelable paint. A two-step anodizing procedure was carried out to improve the morphological features (*i.e.*, degree of pore order, removal of the initiation layer) of the anodic oxide layers.[26] Both steps were carried out in the agitated (750 rpm) ethylene glycol-based (Sigma-Aldrich) electrolyte consisting of deionized water (3% vol.) and NH_4F (0.15 M, Sigma-Aldrich). The process was carried out using a DC power supply (Velleman LABPS6005SM) set to 60 V, in a two-electrode cell with a platinum counter electrode. The oxide layer formed in the first 10 min anodizing step was removed from the Ti substrate by sonication in water. The thickness of the nanotube layers was adjusted by the anodizing time of the 2nd step conducted between 10–30 minutes. After anodizing, samples were washed in ethanol and dried in a nitrogen stream. Thermal annealing in air at 450 °C for 1 h was performed in a muffle furnace to convert the amorphous nanotubes to anatase structure.

Crystalline TiO_2 nanotubes on the Ti substrate (TNT–Ti) obtained in the previous step were subjected to a third anodizing step that forms a thin amorphous TiO_2 layer underneath. For this purpose, the same electrolyte as before was used, however, the anodizing potential was reduced to 15 V and the time to 1 minute.

The TNT–Ti layers were used for electrodeposition of AuNWs inside the tubes and a thin flakes-like morphology of the Au film on the top of the oxide film. The electrochemical deposition was carried out from a cyanide-based plating solution (bright electroless gold plating solution, Sigma-Aldrich) for 2.5 h at a current density of 1 mA cm^{-2}, at room temperature. The process was conducted in a three-electrode system (Ag/AgCl reference electrode and Pt counter electrode) and controlled by a Bio-Logic VMP3 potentiostat/galvanostat.

Afterwards, the structure composed of Au deposited into TNTs attached to the Ti substrate was immersed overnight in a 30% aqueous H_2O_2 solution (Sigma-Aldrich) at room temperature. In this way, the thin amorphous titanium dioxide formed in the third step between the TNTs and Ti substrate has been etched. The result was a self-standing TNT membrane on AuNW array (TNT–AuNW).

Materials characterization

A JEOL JSM-6060 scanning electron microscope (SEM) was used to examine the morphology of fabricated photoelectrodes.

High-resolution transmission electron microscopy (HRTEM), high-angle annular dark-field scanning transmission electron microscopy (HAADF-STEM), selected area electron diffraction (SAED) patterns, and energy dispersive X-ray analysis (EDX) measurements were acquired with a FEI Talos F200S scanning/transmission electron microscope (S/TEM) operated at 200 kV. Geometrical features were measured from TEM images using ImageJ software.

X-ray powder diffraction patterns were recorded using a STOE MP diffractometer equipped with a Mo K_α source (λ = 0.07093 nm). Photoelectrochemical and electrochemical tests were carried out in a Teflon cell with a quartz window in a three-electrode system, where TNT–Ti or TNT–AuNW materials were used as working electrodes (WE), a platinum foil as a counter electrode (CE), a Ag/AgCl/KCl (3 M KCl) electrode as a reference electrode (RE), and a 0.1 M Na_2SO_4 solution as electrolyte.

Photocurrent transients were recorded under chopped light illumination (light on/off 10/10 s) with a 365 nm (50 mW cm^{-2}) LED source (ThorLabs) and registered with a Bio-Logic VMP3 potentiostat/galvanostat. The power of the LED has been defined with a power and energy meter (PM100D, ThorLabs).

For the incident photon to current efficiency (IPCE) determination, the generated photocurrents were measured using a photoelectric spectrometer equipped with a 150 W xenon arc lamp (Instytut Fotonowy, Krakow, Poland) and combined with a potentiostat (Instytut Fotonowy, Poland). 3D photocurrent maps were measured in the range of 200–500 nm (with a 5 nm wavelength step) and at 0.05 V to 1.25 V *vs.* RHE (with a 100 mV potential step). A pulse illumination of 10 s light and 20 s dark cycles was used at each potential. The IPCE was calculated based on the following formula (1):

$$\mathrm{IPCE}(\lambda)\ [\%] = 1240\left[\mathrm{W\ nm}\ A^{-1}\right]\frac{J_p(\lambda)\left[\mathrm{A\ m^{-2}}\right]}{\lambda\ [\mathrm{nm}]\cdot P(\lambda)\ [\mathrm{W\ m^{-2}}]} \times 100 \quad (1)$$

where $J_p(\lambda)$ is the photocurrent density at the wavelength λ, and $P(\lambda)$ is the incident power density of light at given wavelength λ.

Considering the fact that TiO_2 is known as an indirect band gap semiconductor, band gaps of the materials were determined from $(\mathrm{IPCE}\cdot h\nu)^{0.5}$ *vs.* $(h\nu)$ plots (Tauc plots) by extrapolating the straight regions of the function and determined from the point of their intersection. For the band gaps determination the IPCE spectra registered at 1.25 V *vs.* RHE have been taken.

The electrochemical impedance spectroscopy (EIS) was performed over a frequency range from 100 kHz to 10 mHz using a 5 mV amplitude sinusoidal signal, without and with UV 365 nm irradiation.

A Mott–Schottky analysis performed in dark was carried out to verify the semiconducting properties of the studied photoanodes. The cascade measurement was conducted in a 50–500 Hz frequency range.

X-ray photoelectron spectroscopy (XPS) spectra were acquired in an ultrahigh vacuum chamber with a base pressure of 10^{-10} mbar, using a Mg X-ray source ($h\nu$ = 1253.6 eV) for excitation. For the ultra-violet photoelectron spectra (UPS), a helium discharge lamp ($h\nu$ = 21.2 eV) was used for excitation, and a bias of −10 V was applied for the secondary electron cut-off (SECO) spectra. The number of photoelectrons as a function of their kinetic energy was measured by an Omicron EA125 hemispherical analyzer, using pass energies of 50 eV for the survey spectra, 20 eV for the XPS detail scans, 10 eV for the valence band spectra and 2 eV for the SECO spectra. The binding energy scales were calibrated by setting the Au $4f_{7/2}$ peak to 84.0 eV for XPS and by setting the center of the Fermi-edge of the gold sample to 0 eV for UPS.

Results

The synthesis of TNT–AuNW

TNT–AuNW electrodes were synthesized by a combination of two techniques, *i.e.* anodizing of Ti, and electrodeposition of metal nanowires, complemented by a detachment of the full system from the metal substrate. It is important to note that our method leads to an extremely large total contact area between the metal and the semiconductor. To the best of our knowledge, this synthesis approach and the resulting material system based on self-standing TNT–AuNWs is presented for the first time.

The synthesis steps are presented in Fig. 1 and macrophotographs of the samples at respective synthesis steps are shown in Fig. S1a–d (ESI†). In order to obtain the light energy harvesting constituent element of the photoelectrode, a series of titania nanotube arrays were grown by two-step electrochemical anodizing of Ti substrates. The two-step synthesis approach (Fig. 1(a)) is crucial to improve morphological features of the nanotubes,[3,27] and therefore ensure stable self-standing membranes. Anodizing was carried out in an ethylene glycol-based electrolyte containing 0.15 M NH_4F and 3% vol. H_2O at 60 V constant potential. The 1st anodizing step was carried out 10 min, whereupon the grown oxide layer was removed by sonication in

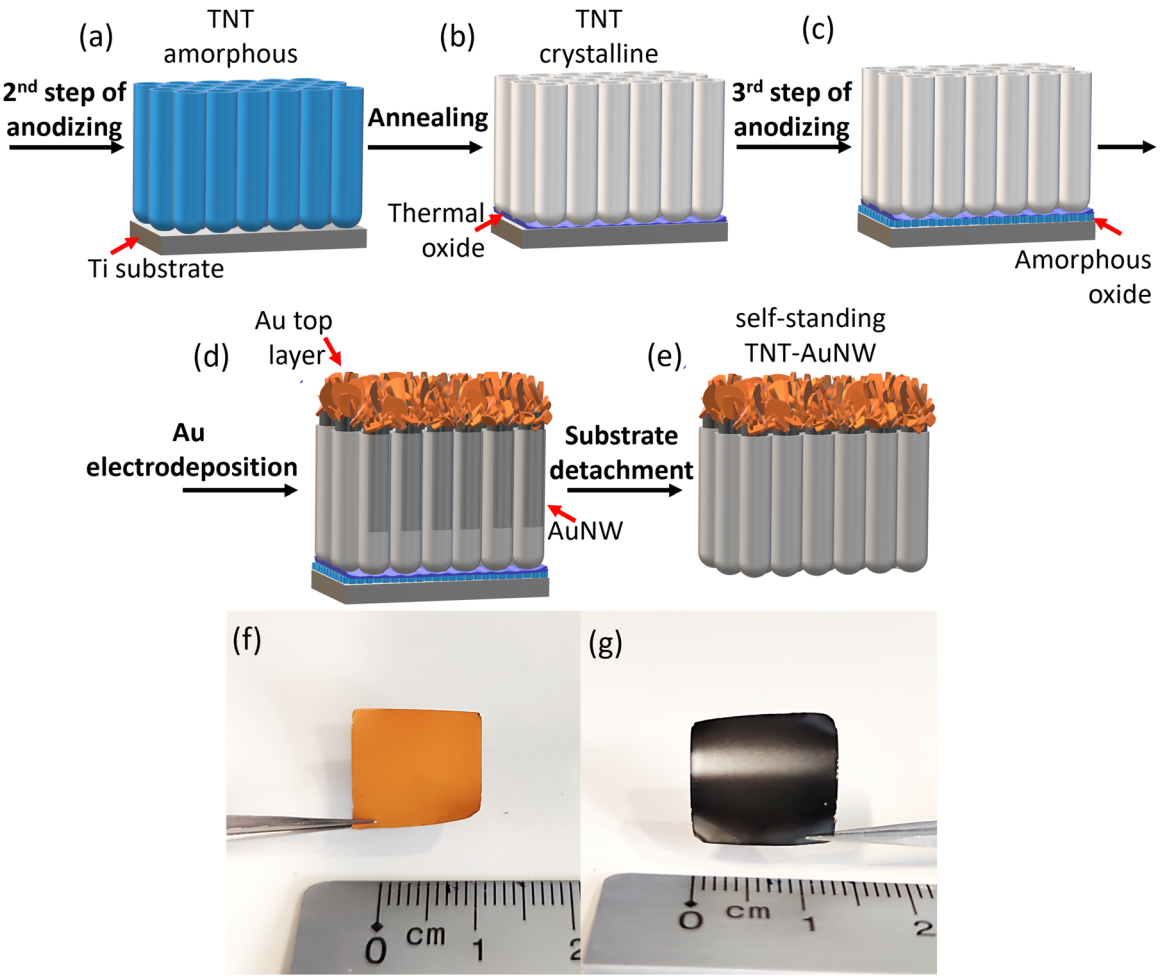

Fig. 1 (a)–(e) Schematic of the fabrication process of highly ordered self-standing titania nanotubes filled with Au nanowires. Macrophotographs of TNT–AuNW (f) from the Au side and (g) TNT side.

water. The thickness of the nanotube layers was adjusted by varying the 2nd anodizing time between 10 and 30 min, resulting in 4.4–10.8 μm thick oxide films (Fig. S2, ESI†). Afterwards, the TNT–Ti was exposed to a thermal treatment in air at 450 °C for 1 h (Fig. S1a, ESI†) to convert amorphous oxide to anatase structure (Fig. 1(b)). Additionally, a thin thermal oxide layer between the nanotubes and substrate has formed.[4]

In the next step, a 3rd anodizing step was carried out to form a thin amorphous layer of TiO_2 (Fig. 1(c)). Such a layer ensures a weak contact spot between crystalline TiO_2 tubes and the Ti substrate. It was previously shown[19] that the combination of post-anodizing annealing followed by a 3rd step anodizing results in uniform detachment of the pristine TiO_2 membrane from the Ti substrate. The conditions applied in this step are the same as previously, however, the applied potential is reduced to 15 V and the time was limited to 1 min. Due to the short anodizing time, a thin oxide layer is formed around concaves left in the metal after the 2nd anodizing step (SEM of the layer morphology shown in Fig. S1e, ESI†).

Afterwards, AuNWs were electrodeposited into the crystalline TiO_2 nanopores (Fig. 1(d) and Fig. S1b, ESI†). As discussed in the introduction, the gold nanowire array can effectively collect the photogenerated charge carriers in TNTs and function as a high interface back contact material. In this work, the electrochemical deposition was carried out from a cyanide-based plating solution for 2.5 h at a current density of 1 mA cm^{-2}. The potential minimum around −1.15 V (*vs.* Ag/AgCl) reached at the beginning of the process represents additional overpotential related to the diffusion into pores, nucleation, and nanowires formation. After about 200 s the potential gradually increases up to approximately −1.05 V. The quasi-steady-state corresponds to the deposition of a relatively compact Au film at the top of TNTs (Fig. S1f, ESI†).

To fabricate free-standing TNT membranes, various approaches can be found in the literature,[19] however, detachment of the assembled TNT–AuNW composite has not been reported yet. The formation of this metal–TNT membrane structure brings strong system stability and allows for successful preparation of as thin as a few micrometers TiO_2 membranes (Fig. S2, ESI†). Here, a chemical etching method has been chosen as the most suitable method for the detachment of the TNT–AuNW system. The thin amorphous titania layer (Fig. S1e, ESI†) formed in the third anodizing step (Fig. 1(c)) is preferentially etched by overnight immersion in 30% H_2O_2, while the crystalline TNT can survive the treatment without any

deterioration (Fig. S1c, ESI†). The TNT–AuNW composite structure was completely lifted-off from the Ti substrate (Fig. S1d, ESI†) resulting in a stable, self-standing thin layer with an orange color on the Au side (Fig. 1(f)) and a black color on the TNT side (Fig. 1(g)).

Morphology and crystal structure

The morphologies of the materials at different stages of the preparation are shown in Fig. 2 and Fig. S2 (ESI†). The TNTs fabricated in a two-step anodizing procedure (Fig. 2(a) and (b)) show a high degree of ordering. The parallel nanotubes have an individual inner diameter of ~100 nm. The tube length is correlated with the duration of the 2nd anodizing step between 10–30 minutes, which results in a 4.4–10.8 μm thickness range (Fig. S2, ESI†). Indeed, the ideal membrane thickness needs to be found for the best compromise between a sufficient light absorption and an electron diffusion length in the nanotubes to minimize charge recombination.

The SEM images of TNT–AuNW (Fig. 2(c)–(f)) show the Au layer (photoanode back contact) with a flake-like structure (Fig. 2(c) and (f)). The top of the TNT–AuNW composite is presented in Fig. 2(e), which shows the typical morphology of TNT bottoms, slightly sintered after annealing. The AuNWs inside the tubes are clearly visible in Fig. 2(d), where the TNTs and Au layers slightly detached from each other after the sample cutting. A more detailed view of the deposition of the AuNWs in TNTs can be seen from HR-TEM results.

From the high-angle annular dark-field scanning transmission electron microscopy (HAADF-STEM) image (Fig. 3(a)) of the AuNW-TNT sample, the structure of AuNWs surrounded by TiO_2 can be easily recognized. This is consistent with the bright-field TEM images, where the phases of Au and TiO_2 can be identified due to their different Z-contrast (Fig. 3(b)).

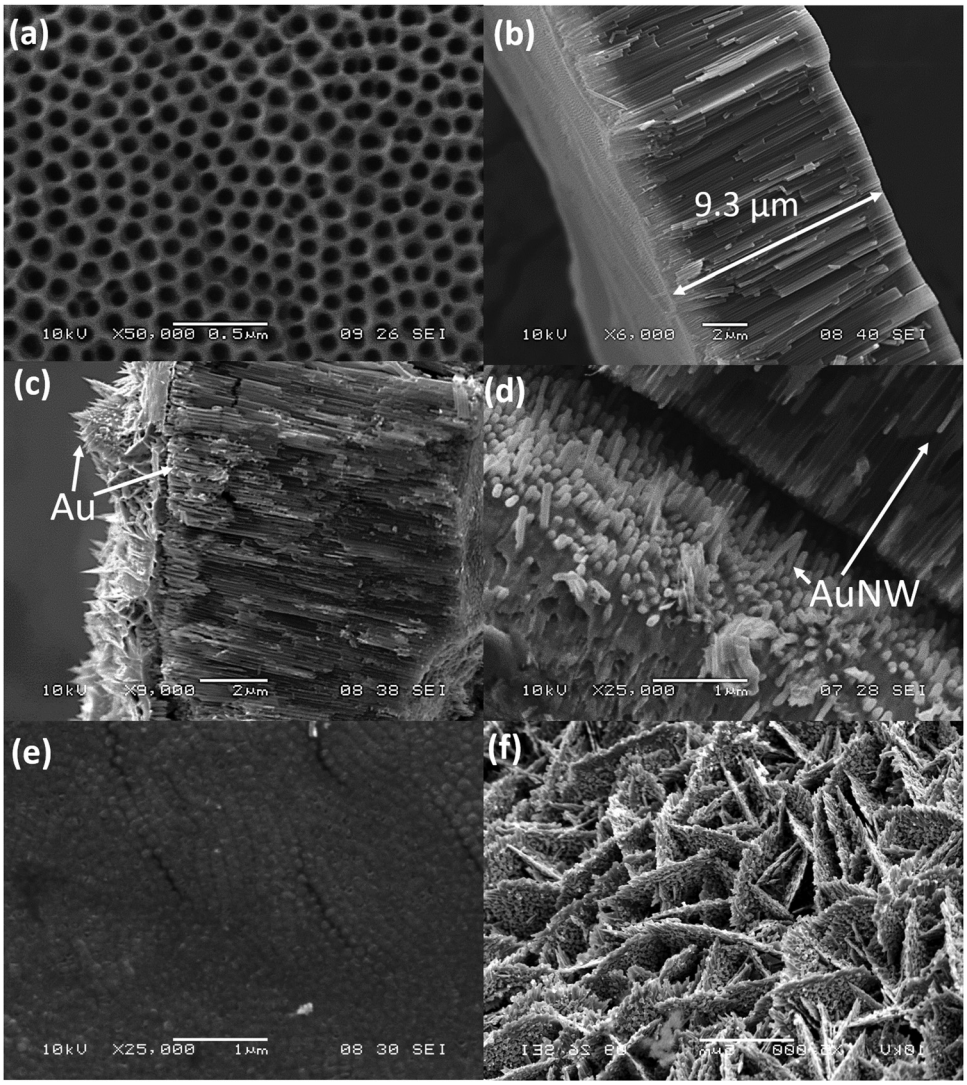

Fig. 2 SEM images of pristine anodic TiO_2 nanotube arrays after 20 minutes of 2nd step anodizing from (a) top view and (b) cross-section; and TNT–AuNW (c) cross-sectional view, (d) interface of AuNWs slightly detached from TNTs due to sample cutting, (e) top of the TNT–AuNW electrode (bottoms of TNTs), (f) flake-like morphology of its Au thin film (back side of the photoanode).

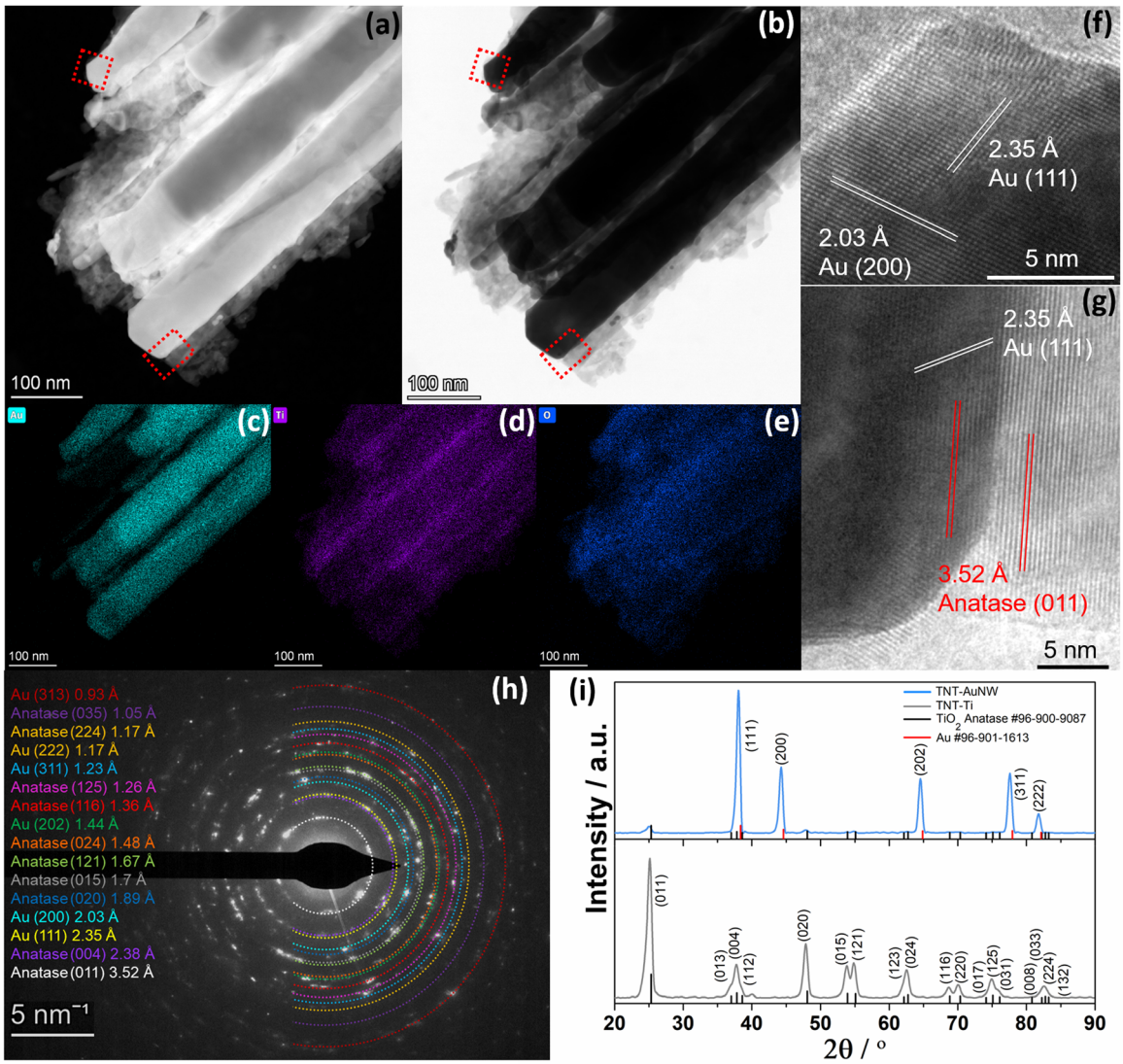

Fig. 3 (a) HAADF-STEM corresponding to (b) bright field HR-TEM and (c)–(e) EDX elemental maps. HRTEM micrographs of (f) exposed AuNW, and (g) AuNW inside TNT. The images were taken from the enlarged areas in figures (a) and (b) in the red square marked places. (h) SAED patterns acquired from the TNT–AuNW sample. (i) XRD patterns for the synthesized TNT–AuNW and pristine TNT samples.

The energy-dispersive X-ray spectroscopy (EDX) elemental mappings corresponding to the HAADF-STEM images confirm the presence of Au in the internal core as well as Ti and O homogenously distributed in the shell layer of the structure (Fig. 3(c)–(e)). Fig. 3(f) shows a HR-TEM image of a part of AuNWs with characteristic lattice fringes (111) with a d spacing of 0.235 nm[28] and (200) with 0.203 nm[29] for fcc Au,[30] while Fig. 3(g) shows less pronounced fringes of Au covered with TiO_2, identified as anatase by the lattice fringes (011) with a d spacing of 0.352 nm.[31] These results clearly evidence the formation of the close contact metal-semiconductor heterostructure.

Further crystallographic information from the samples was obtained from the selected area electron diffraction (SAED) and X-ray diffraction spectra. The corresponding Debye–Scherrer rings in the SAED patterns recorded for the TNT–AuNW samples confirm the polycrystalline character of all materials (Fig. 3(h)). The main Debye–Scherrer rings for TiO_2 in the samples correspond to the (011), (004), (020), (015), (121), (024), (116), (125), (224), and (035) planes in anatase (tetragonal crystal system ICDD: 96-900-9087), while the rings from Au represent planes (111), (200), (202), (311), (222), and (313) assigned to fcc Au (ICDD: 96-901-1613). These findings are in line with X-ray diffraction patterns obtained from TNT (grey line) and TNT–AuNW (blue line) samples that further confirmed the Au deposition by the presence of distinctive crystalline phases of TiO_2 anatase before deposition and additional Au reflections after electrodeposition. It is clear that the crystallites of Au nanowires are much larger than the TiO_2 crystallites in the TNT–AuNW sample as reflected in the significant differences in respective peaks intensity.

Photoelectrochemical water splitting on TNT–AuNW electrodes

The specific combination of composition and architecture of the fabricated electrodes makes them promising candidates for

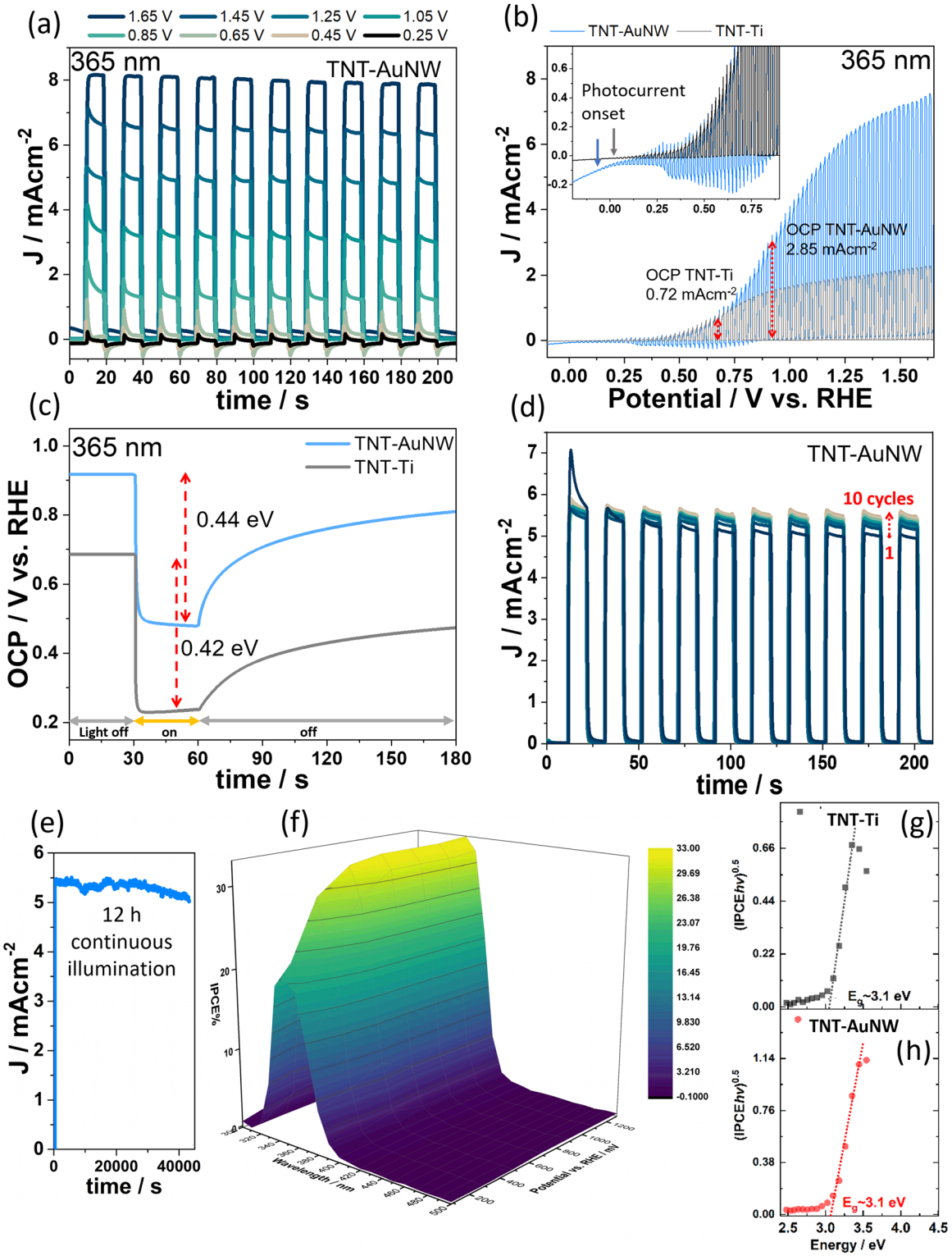

Fig. 4 (a) Transient photocurrent responses of the TNT–AuNW photoanode measured under 365 nm LED illumination and varied constant potentials in the range from 0.25 to 1.65 V *vs.* RHE in a 0.1 M Na_2SO_4 solution. (b) Linear sweep voltammograms registered under chopped light illumination (365 nm) from TNT–AuNW and TNT–Ti reference samples. (c) Open circuit potential (OCP) of the photoanodes measured under dark and UV illumination. Stability test of the TNT–AuNW electrode under (d) chopped light and (e) continuous 12 h illumination with 365 nm. (f) IPCE 3D photoactivity map measured for TNT–AuNW. Evaluated band gaps of (g) TNT on Ti and (h) TNT on AuNW from IPCE data given in Fig. S5 (ESI†).

stable and high-performance solar energy harvesting materials, here tested by photoelectrochemical water splitting. As the photoelectrochemical performance is the result of a trade-off between light absorption and electron diffusion length, the

optimal thickness of the TiO_2 membrane in the TNT–AuNW electrodes was determined in the PEC WS tests under chopped UV light (365 nm) illumination and at positive 1.25 V bias *vs.* RHE. Fig. S3 (ESI†) shows the photocurrents recorded on electrodes of varied thicknesses between 4.4–10.8 μm (Fig. 2 and Fig. S2, ESI†). It was found that PEC efficiency is increasing with the TiO_2 layer thickness up to 9.3 μm (20 minutes of anodizing, Fig. 2), reaching a current density of 5.4 mA cm^{-2}, and then decays back to a lower value for a thicker semiconductor layer. This is the result of a trade-off between light harvesting ability (material thick enough to absorb the vast majority of photons) and increasing distance for charges to travel through the layer (the longer the distance excitons must travel the higher the probability they will recombine before reaching the electrodes surface).[32,33] For more details see ESI.†

The sample of optimal thickness has been used for further PEC testing. As can be seen from Fig. 4(a), the photocurrents generated at different bias voltages from 0.25 V to 1.65 V *vs.* RHE are very stable over time in the whole range of potentials tested, with the highest photocurrent density of 8 mA cm^{-2} for 1.65 V bias, which is about four times higher in comparison to the TNT–Ti reference sample (Fig. 4(b) and Fig. S4a, ESI†).

To understand the difference in the photocurrent generation efficiency of TNT–Ti and TNT–AuNW photoanodes, the photocurrent spectra were registered in linear sweep mode from 1.65 V to −0.15 V (Fig. 4(b)). These results show that the TNT–AuNW photocurrent onset potential is located at the value of a more negative potential than for TNT–Ti (−0.1 V *vs.* 0.05 V respectively). In the region of the negative potential, small cathodic transients have been registered for the TNT–AuNW, probably due to Au being a catalyst for H_2 evolution, which can facilitate the reduction reaction on the electrode surface. The strong contrast between the two photoelectrodes is revealed by the comparison of the potential-dependence performance of the PEC processes. TNT–Ti reaches almost a plateau already from 0.9 V, while TNT–AuNW shows a systematic increase of photocurrent up to 1.65 V *vs.* RHE.

To substantiate the origin of the enhanced activity of TNT–AuNW, the open circuit potentials (OCP) of both electrodes have been tested in the dark and under UV illumination (365 nm) (Fig. 4(c)). It can be seen that the relative change of the electrodes potentials caused by light illumination is almost the same. Apparently, the number of photogenerated electrons is almost equal regardless of the type of photoelectrode type, and depends only on the properties of the TiO_2 layer as the light absorber. The potential change to more negative values during illumination is characteristic for n-type semiconductors.[34] Since the number of photogenerated charges is equivalent, these results prove that the reason for a better performance of the TNT–AuNW is rather faster electron transfer through the metal NWs and better charge separation due to the Schottky barrier, while TNT–Ti suffers from high electron–hole recombination. Note that the results presented in Fig. 4(c) show also that the TNT–AuNW has about 0.2 V higher OCP than TNT–Ti, which means that even without applying an external bias to the system, the photocurrents from TNT–AuNW are four times higher than from TNT–Ti (marked in Fig. 4(b)).

Very importantly, the TNT–AuNW photoanode also shows very good stability. The long-time PEC performance, which was tested at a constant potential of 1.25 V (*vs.* RHE), shows that after ten measurements, each consisting of ten light on/off cycles (a total of one hundred repetitions), the photocurrent increases by about 0.56 mA cm^{-2} and after that it remains stable (Fig. 4(d)). This could be an effect of *e.g.*, metal-semiconductor junction reduction, as point defects at the interface have a distinct influence on the PEC system performance.[35] Moreover, long-term PEC performance confirmed full stability of the photoanode over 12 h of continuous illumination under 365 nm (Fig. 4(e)). Small photocurrent fluctuations are caused by oxygen bubbles sticking to the quartz window and slightly dispersing the incident light. Furthermore, once the TNT–AuNW photoelectrode reached the final photocurrent conversion efficiency, it stays at the same level even after a week or month of storage in air (Fig. S4b, ESI†).

To further characterize the photoelectrochemical properties of TNT–AuNW, an ICPE 3D map has been calculated (Fig. 4(f)) for wider wavelength (300–500 nm) and potential ranges (0.05 to 1.25 V *vs.* RHE). Although the deep black color of the photoanode, probably coming from nanostructured Au plasmonic effect of the material,[36] the highest IPCE of ∼5% has been reached particularly for short wavelengths *e.g.*, 350 nm (IPCE for 1.25 V shown in ESI,† Fig. S5). Only UV light absorption (<400 nm) translates into photocurrent, also indicating that the band gap has not been narrowed. Band gap estimations provided based on the Tauc plot of the Kubelka–Munk function calculated for an indirect transition in anatase TiO_2 (Fig. 4(g) and (h)) suggest that the E_g of TNT on AuNW is equivalent to that of TNT–Ti, *i.e.*, *ca.* 3.1 eV, typical for anatase.[37] In other words, there are no states contributing to the photocurrent in the band gap related to the presence of AuNW.

Characterization of electronic properties of nanostructured Au/TiO_2 interface

Photoelectron spectroscopy measurements were conducted to confirm the sample composition and to determine the energy level alignment at the Au/TiO_2 heterojunction. The survey spectra of the Au reference sample, TNT–Ti and TNT–AuNW are shown in Fig. S6 (ESI†). All expected elements (Au, Ti, O) are present plus adventitious carbon stemming from air exposure of the samples. The UPS spectra and the XPS detail scans are shown in Fig. 5. The SECO spectra yield work functions (the energy of Fermi level determined with respect to the vacuum) of ∼4.7 eV for the gold reference sample, a common value for air-exposed gold,[38,39] and ∼3.8 eV for the TNT–Ti sample, as also observed before for *ex situ* prepared TiO_2 samples.[40] The TNT–AuNW sample has a work function of ∼4.5 eV, only slightly lower than the gold reference sample, indicating an electron transfer from the n-type TiO_2 shell to the Au nanowire and a concomitant formation of a Schottky-barrier between the two, as expected from the work functions of the pristine materials. This increase in work function is in line with both

shifts of the TiO_2 valence band (Fig. 5(b)) and the Ti 2p core levels to lower binding energies (Fig. 5(c)) by ~0.6 eV. The valence band measurements represent the difference between the energy of the Fermi level and the valence band (Fig. 5(e)). The Ti 2p core level consists of only one pair of peaks for both the pristine TiO_2 and the Au/TiO_2 samples, with a Ti $2p_{3/2}$ binding energy of 459.59 eV and 459.06 eV, respectively, and a spin–orbit splitting of 5.7 eV, indicating the presence of Ti^{4+} only.[41–43] A small signal of the Au 4f core levels is still detectable for the TiO_2/Au heterostructure, showing no shift in energy compared to the Au reference sample, which indicates that the Au is chemically unaltered. With all this information the energy level diagram of the Au/TiO_2 heterojunction has been drawn as shown in Fig. 5(e). The TiO_2 forms a Schottky-barrier around the Au nanowires, facilitating charge separation.

The PES results are in line with the Mott–Schottky analysis, which shows a strong flat band potential shift (approximately CB position) at the TiO_2/electrolyte interface in the TNT–AuNW composite[44] as discussed in the following section.

Charge transport and semiconducting characteristics of TNT–AuNW electrode

In order to assess the impact of the TNT and AuNW nanostructured interface on the PEC efficiency, the charge carrier kinetics have been explored by electrochemical impedance spectroscopy (EIS), both in the dark and under UV light irradiation. The data in Fig. 6 show that TNT–AuNW has a much higher conductivity, represented by a smaller semicircle radius in the Nyquist plots, and an order of magnitude lower impedance modulus for low frequencies ($|Z|_{10mHz}$), as seen from the Bode representation, in comparison to pristine TNT, both in dark and under light illumination. The respective increase of conductivity due to light illumination is similar for both electrodes, because the number of photogenerated electrons is equal and proportional to the thickness of the TiO_2 layer. This is in line with the results of OCP measurements of the electrodes in dark and under light illumination, presenting almost the same potential change (Fig. 4).

Based on the shape interpretation of Nyquist and Bode plots equivalent circuits elements have been selected and their suitability has been confirmed by fitting the experimental data with the model systems according to the equivalent circuit presented in insets in Fig. 6(b) and (e). The corresponding electrochemical parameters of the elements used to fit the experimental data are presented in Table S1 (ESI†). All the models include R_s which accounts for the resistance of the electrolyte. In the phase angle plot (Fig. 6(c)) can be seen that the TNT–Ti in the dark shows the presence of two time constants (two distinct peaks), which can be attributed to phenomena at the electrolyte/electrode interface and a space charge layer at the semiconductor–Ti metal interface.[45] Respectively, R_{ct} represents a charge transfer resistance in parallel to the constant phase element (Q_{dl}) describing the double-layer capacitance, connected in series with Q_{SC} and R_{SC} ascribed to a space charge region in the semiconductor TNT–Ti electrode. Because both peaks show a phase angle smaller than 90°,[46] typical for a perfect capacitor, constant phase elements (Q) have been used to account for the non-ideal capacitive behavior of the system.

Under light illumination of TNT–Ti one time constant in the high frequency, representing the charge carrier kinetics in the space charge region, has vanished. This can be assigned to the increase of the electron concentration in the CB that facilitates the flow of electric current through the system. Interestingly, in the case of TNT–AuNW, there is no space charge capacitance even in the dark. These findings are in line with reports on a fast electron extraction by noble metals that prevents accumulation in the TiO_2 semiconductor.[6,45] Under

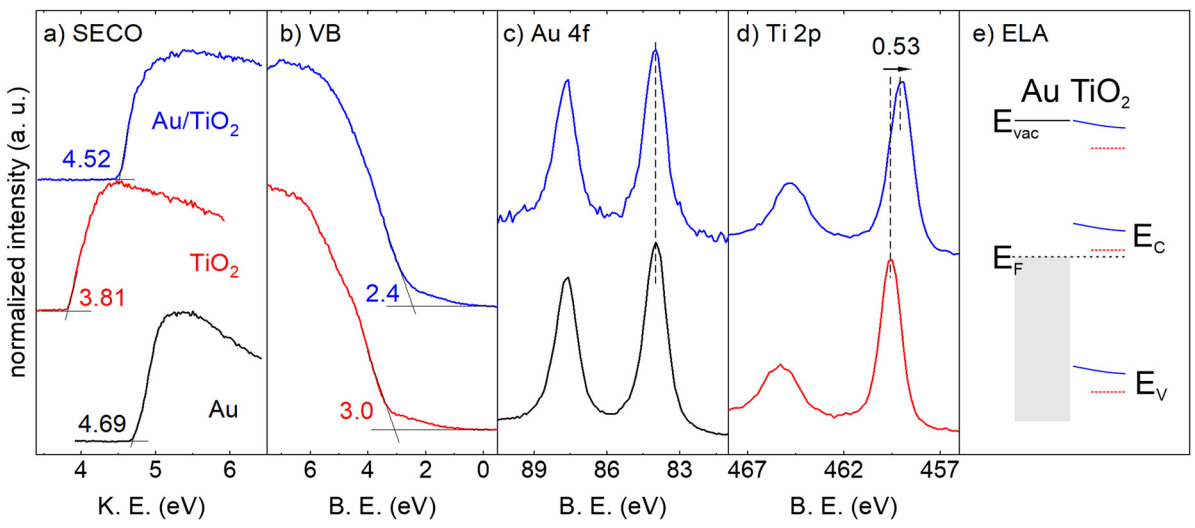

Fig. 5 (a) Secondary electron cutoff (SECO) (b) valence band (VB), (c) Au 4f, and (d) Ti 2p core levels of TNT–Ti, TNT–AuNW, and Au electrodeposited on the Ti substrate as reference. All TiO_2 core levels as well as the VB onset are shifted by 0.6 ± 0.1 eV to lower binding energies for the TNT–AuNW compared to the pristine TNT–Ti. (e) From the PES measurements derived energy band diagram of the TNT–AuNW heterojunction. The red dashed lines indicate the energy levels of the pristine TNT–Ti.

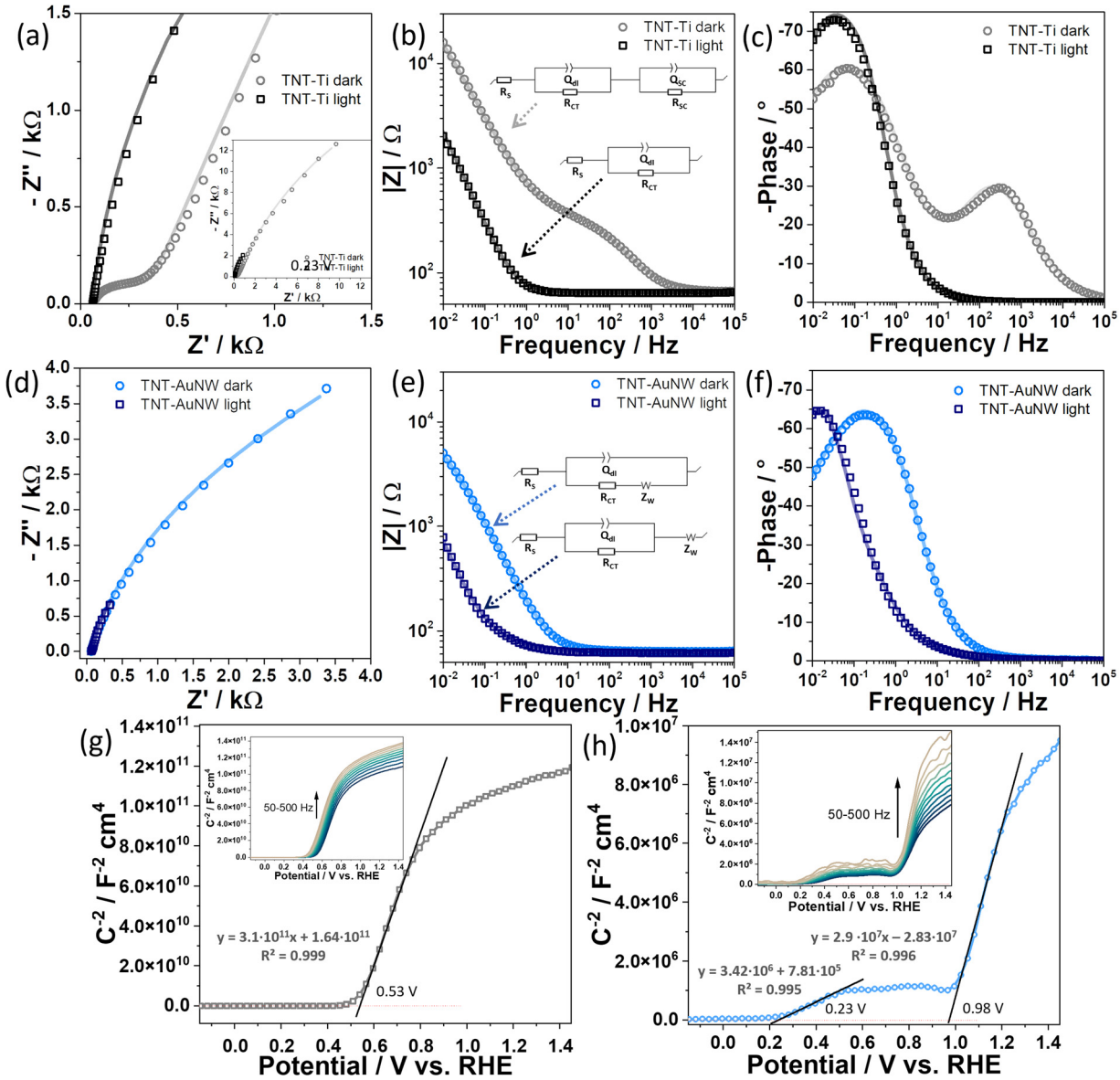

Fig. 6 (a and d) Nyquist and (b, c and e, f) Bode plots fitted with simulated equivalent circuits determined for TNT–Ti and TNT–AuNW, respectively. Empty symbols correspond to the experimental data; sold line correspond to the fitting obtained with equivalent circuits presented in (b and e). Mott–Schottky plots measured at a frequency range of 50–500 Hz for (g) TNT–Ti and (h) TNT–AuNW electrodes.

illumination, the presence of AuNW causes a shift toward higher frequencies of the phase angle peak associated with the electrochemical double layer. Here, also the Randles cell models have been supplemented with the Warburg impedance (Z_W) component recognized based on a characteristic trend in the Nyquist plot, namely, a linear increase in Z values at low frequencies, with $\phi = 45°$.[47] Because the reaction that takes place at the TNT–AuNW electrode is very efficient, the contribution of ion diffusion to the electrode surface has a significant contribution to the process. Under light illumination, the influence of the Warburg element is pronounced even more as the mass transfer control dominates the process.[48]

The Mott–Schottky analysis was performed in order to identify the depletion regions in the TNT–Ti and TNT–AuNW photoanode materials. A linear dependence of C_{sc}^{-2} on the applied potential with positive slopes (Fig. 6(g) and (h)) indicates n-type semiconducting behavior. Clearly, the self-standing titania membrane filled with Au nanowires (TNT–AuNW) confirms the presence of two depletion regions (semiconductor/metal and semiconductor/electrolyte barriers) while the reference TNT–Ti shows only one interfacial capacitance of the electric double layer at the semiconductor/electrolyte interface.[49] The second dielectric barrier placed at 0.98 V (*vs.* RHE) is the Schottky barrier between TiO_2 and AuNW. The potential region limited by the two barriers closely overlaps with the region at which the cathodic spikes are formed in the PEC-LSV experiment (Fig. 4(b)) as the result of inefficient current flow through the composite material. Nevertheless, in practice, the barrier is rather insignificant since

the potential of the Schottky barrier is only slightly higher than the dark OPC of the electrode (Fig. 4(c)). Moreover, comparison of the slopes determined for linear parts of the registered Mott–Schottky dependencies are reduced several orders of magnitude due to the presence of AuNW that provides a high carrier concentration in the electrode. A small local minimum preceding the region of the Schottky barrier (successive positive and negative slopes) represents the build-in potential at the interface, analog to the one in the n–p junction, which is interpreted as the reason for enhanced charge separation.[11,22–24] Importantly, also the flat band potential of TNT–AuNW is shifted to a more negative value (0.23 V *vs.* RHE) than for anodic TiO_2 (0.53 V). This observation is also in line with the offset potentials determined from LSV photocurrent tests (Fig. 4(b)).

This electrochemical characterization clearly shows that under a small forward bias (reduction of the Schottky barrier) and under illumination (higher electron concentration in the CB) an electron transfer through the AuNWs is strongly facilitated in comparison to the TNTs on the Ti metal substrate.

Conclusions

In this work, we have introduced an original synthesis approach, of nanostructured self-standing TNT membranes (light absorber) filled with AuNW arrays on a thin Au film (the electrons collector). It has been proved that the proposed core–shell structure, leading to a large surface area of the metal-semiconductor contact, yields a distinct increase of the photocurrent production (8 mA cm^{-2} at 1.65 V *vs.* RHE), four times higher than for TNT–Ti obtained under the same anodizing conditions. The IPCE under UV light illumination reaches 35%. A combination of selected constitutional materials of the composite (Au as a noble metal and TiO_2 as a very stable semiconductor) ensures a stable long-time performance (no loss after 100 repetitions, under continuous illumination for 12 h and after one-month storage in air).

Photoelectron spectroscopy measurements (UPS and XPS) confirmed that the band alignment results in a Schottky-barrier formation at the TNT–AuNW interface, which is rectifying for electrons and ohmic for holes, while the electrochemical characterization showed that the specific architecture of the photoanode supports electron separation by the Schottky type contact and fast electron transport through the Au nanowires.

We find this type of heterojunction architecture to be an innovative platform for efficient photoelectrochemical water splitting under UV light illumination, with potential for further modifications, particularly extension into the visible light regime by *e.g.* doping of TiO_2.

Author contributions

EW: conceptualization, data curation, formal analysis, funding acquisition, investigation, methodology, supervision, validation, visualization, writing – original draft, writing – review & editing; TS: formal analysis, investigation, visualization, writing – original draft, writing – review & editing; KS: formal analysis, investigation, visualization, writing – original draft, writing – review & editing; GS: funding acquisition, resources, supervision, writing – review & editing; NK: resources, supervision, writing – review & editing; NP: resources, supervision, writing – review & editing.

Conflicts of interest

There are no conflicts to declare.

Acknowledgements

E. W. would like to acknowledge Alexander von Humboldt Foundation, Bonn, Germany, for funding the postdoctoral fellowship, and the Polish National Agency For Academic Exchange, Polish Returns Programme (Project no. BPN/PPO/2021/1/00002), and the National Science Centre, Poland (Project no. 2022/01/1/ST5/00019) for financial support of the project. G. S. would like to acknowledge the National Science Centre, Poland (Project no. 2016/23/B/ST5/00790). The authors thank C. Erdmann for performing the transmission electron microscopy measurements.

References

1 E. Wierzbicka, X. Zhou, N. Denisov, J. E. Yoo, D. Fehn, N. Liu, K. Meyer and P. Schmuki, *ChemSusChem*, 2019, **12**, 1900–1905.
2 E. Wierzbicka, B. Osuagwu, N. Denisov, D. Fehn, K. Meyer and P. Schmuki, *IOP Conf. Ser.: Mater. Sci. Eng.*, 2020, **908**, 012001.
3 J. Kapusta-Kołodziej, K. Syrek, A. Pawlik, M. Jarosz, O. Tynkevych and G. D. Sulka, *Appl. Surf. Sci.*, 2017, **396**, 1119–1129.
4 J. E. Yoo and P. Schmuki, *J. Electrochem. Soc.*, 2019, **166**, C3389–C3398.
5 H. C. Liang, X. Z. Li and J. Nowotny, *Solid State Phenom.*, 2010, **162**, 295–328.
6 K. Syrek, J. Grudzień, A. Sennik-Kubiec, A. Brudzisz and G. D. Sulka, *J. Nanomater.*, 2019, **2019**, 9208734.
7 V. C. Anitha, R. Zazpe, M. Krbal, J. E. Yoo, H. Sopha, J. Prikryl, G. Cha, S. Slang, P. Schmuki and J. M. Macak, *J. Catal.*, 2018, **365**, 86–93.
8 E. Wierzbicka, M. Domaschke, N. Denisov, D. Fehn, I. Hwang, M. Kaufmann, B. Kunstmann, J. Schmidt, K. Meyer, W. Peukert and P. Schmuki, *ACS Appl. Energy Mater.*, 2019, **2**, 8399–8404.
9 F. Shahvaranfard, P. Ghigna, A. Minguzzi, E. Wierzbicka, P. Schmuki and M. Altomare, *ACS Appl. Mater. Interfaces*, 2020, **12**, 38211–38221.
10 A. Meng, L. Zhang, B. Cheng and J. Yu, *Adv. Mater.*, 2019, **31**, 1807660.
11 M. S. Arshad, Š. Trafela, K. Ž. Rožman, J. Kovač, P. Djinović and A. Pintar, *J. Mater. Chem. C*, 2017, **5**, 10509–10516.

12 G. Žerjav, J. Zavašnik, J. Kovač and A. Pintar, *Appl. Surf. Sci.*, 2021, **543**, 148799.
13 M. R. Khan, T. W. Chuan, A. Yousuf, M. N. K. Chowdhury and C. K. Cheng, *Catal. Sci. Technol.*, 2015, **5**, 2522–2531.
14 L. G. Devi and R. Kavitha, *Appl. Surf. Sci.*, 2016, **360**, 601–622.
15 A. Naldoni, T. Montini, F. Malara, M. M. Mróz, A. Beltram, T. Virgili, C. L. Boldrini, M. Marelli, I. Romero-Ocaña, J. J. Delgado, V. Dal Santo and P. Fornasiero, *ACS Catal.*, 2017, **7**, 1270–1278.
16 S. Hejazi, S. Mohajernia, B. Osuagwu, G. Zoppellaro, P. Andryskova, O. Tomanec, S. Kment, R. Zbořil and P. Schmuki, *Adv. Mater.*, 2020, **32**, 1908505.
17 Y. Liu, E. Wierzbicka, A. Springer, N. Pinna and Y. Wang, *J. Phys. Chem. C*, 2022, **126**, 1778–1784.
18 Y. Wang, X. H. Liu, Q. Wang, M. Quick, S. A. Kovalenko, Q. Y. Chen, N. Koch and N. Pinna, *Angew. Chem., Int. Ed.*, 2020, **59**, 7748–7754.
19 G. Liu, K. Wang, N. Hoivik and H. Jakobsen, *Sol. Energy Mater. Sol. Cells*, 2012, **98**, 24–38.
20 F. Flores, J. Sanchez-Dehesa and F. Guinea, *J. Phys.*, 1984, **45**, 401–407.
21 S. K. Ravi, W. Sun, D. K. Nandakumar, Y. Zhang and S. C. Tan, *Sci. Adv.*, 2018, **4**, 1–9.
22 S. Kawasaki, R. Takahashi, T. Yamamoto, M. Kobayashi, H. Kumigashira, J. Yoshinobu, F. Komori, A. Kudo and M. Lippmaa, *Nat. Commun.*, 2016, **7**, 1–3.
23 H. Frohlich, *Proc. R. Soc. London, Ser. A*, 1977, **354**, 101–118.
24 X. Ren, P. Gao, X. Kong, R. Jiang, P. Yang, Y. Chen, Q. Chi and B. Li, *J. Colloid Interface Sci.*, 2018, **530**, 1–8.
25 S. Mori, K. Sunahara, Y. Fukai, T. Kanzaki, Y. Wada and S. Yanagida, *J. Phys. Chem. C*, 2008, **112**, 20505–20509.
26 A. Mazare, *ACS Appl. Mater. Interfaces*, 2022, **14**, 14837–14841.
27 Y. Fu and A. Mo, *Nanoscale Res. Lett.*, 2018, **13**, 187.
28 J. Zhou, Z. Fu, D. Gao, F. Gao, N. Li, X. Zhao, Y. Liu, Z. Wang and G. Wang, *J. Nanomater.*, 2013, **2013**, 346274.
29 Q. Ding, Z. Kang, X. He, M. Wang, M. Lin, H. Lin and D. P. Yang, *Microchim. Acta*, 2019, **186**, 1–9.
30 S. Han, G. J. Xia, C. Cai, Q. Wang, Y. G. Wang, M. Gu and J. Li, *Nat. Commun.*, 2020, **11**, 1–10.
31 S. Chen, A. M. Abdel-Mageed, D. Li, J. Bansmann, S. Cisneros, J. Biskupek, W. Huang and R. J. Behm, *Angew. Chem., Int. Ed.*, 2019, **58**, 10732–10736.
32 G. Cha, P. Schmuki and M. Altomare, *Electrochim. Acta*, 2017, **258**, 302–310.
33 R. P. Lynch, A. Ghicov and P. Schmuki, *J. Electrochem. Soc.*, 2010, **157**, G76.
34 H. Li, X. Wang, L. Zhang and B. Hou, *Nanotechnology*, 2015, **26**, 155704.
35 H. J. Snaith and M. Grätzel, *Adv. Mater.*, 2006, **18**, 1910–1914.
36 H. Yan, B. Liu, G. Fan, A. Glamazda, F. Ludwig, D. Wulferding, M. Schilling, R. Gao and P. Lemmens, *Phys. E*, 2020, **121**, 114092.
37 T. A. Kandiel, A. Feldhoff, L. Robben, R. Dillert and D. W. Bahnemann, *Chem. Mater.*, 2010, **22**, 2050–2060.
38 M. Fahlman, A. Crispin, X. Crispin, S. K. M. Henze, M. P. de Jong, W. Osikowicz, C. Tengstedt and W. R. Salaneck, *J. Phys.: Condens. Matter*, 2007, **19**, 183202.
39 A. Kahn, *Mater. Horiz.*, 2016, **3**, 7–10.
40 S. Kashiwaya, J. Morasch, V. Streibel, T. Toupance, W. Jaegermann and A. Klein, *Surfaces*, 2018, **1**, 73–89.
41 N. Kruse and S. Chenakin, *Appl. Catal., A*, 2011, **391**, 367–376.
42 M. Wagstaffe, H. Hussain, M. J. Acres, R. Jones, K. L. Syres and A. G. Thomas, *J. Phys. Chem. C*, 2017, **121**, 21383–21389.
43 J. T. Mayer, U. Diebold, T. E. Madey and E. Garfunkel, *J. Electron Spectrosc. Relat. Phenom.*, 1995, **73**, 1–11.
44 M. Sołtys-Mróz, K. Syrek, J. Pierzchała, E. Wiercigroch, K. Malek and G. D. Sulka, *Appl. Surf. Sci.*, 2020, **517**, 146195.
45 M. Altomare, N. T. Nguyen, S. Hejazi and P. Schmuki, *Adv. Funct. Mater.*, 2018, **28**, 1–9.
46 U. Rammelt and G. Reinhard, *Electrochim. Acta*, 1990, **35**, 1045–1049.
47 E. von Hauff, *J. Phys. Chem. C*, 2019, **123**, 11329–11346.
48 R. García-González and M. T. Fernández Abedul, *Laboratory Methods in Dynamic Electroanalysis*, 2020, pp. 119–126.
49 F. Cardon and W. P. Gomes, *J. Phys. D: Appl. Phys.*, 1978, **11**, L63–L67.

